AIAA AVIATION Forum
August 2-6, 2021, VIRTUAL EVENT
AIAA AVIATION 2021 FORUM

10.2514/6.2021-3211

Check for updates

Nailed It: Autonomous Roofing with a Nailgun-Equipped Octocopter

Matthew Romano*, Yuxin Chen†, Prince Kuevor‡, Owen Marshall§, and Ella Atkins ¶
University of Michigan, Ann Arbor, MI, 48109

This paper presents the first demonstration of autonomous roofing with a multicopter. A DJI S1000 octocopter equipped with an off-the-shelf nailgun was used to secure shingles on an adjustable-slope roof mock-up. The nailgun was modified to allow safe, autonomous triggering from the multicopter through tooltip compression feedback. A mount was designed to adjust the angle to match representative roof slopes. An open-source octocopter autopilot facilitated controller adaptation for the roofing application. An autonomous nailing sequence was developed using smooth trajectories designed to apply prescribed contact forces for reliable nail deployment. Experimental results showed that the system is capable of nailing within a required three centimeter vertical gap on the shingle at 30° roof slope. Extensions to achieve a complete autonomous roofing system are discussed as future work.

Downloaded by Matthew Romano on July 29, 2021 | http://arc.aiaa.org | DOI: 10.2514/6.2021-3211

I. Introduction

Unmanned aircraft systems (UAS) have been used for a variety of perception tasks including aerial photography, surveillance, and forest fire monitoring. More recently, physical manipulation applications have been explored such as grasping, perching, and tethered payload carriage [1][2][3]. These emerging applications have the potential to save lives and create significant value since UAS can access sites that are hazardous and difficult for people (and ground robots) to reach. One such hazardous application is roofing, the fourth most dangerous job in the United States at 51.5 fatalities per 100,000 full-time roofers [4]. Roofing is labor intensive and provides an array of physical manipulation tasks to explore. This paper presents the first autonomous experimental demonstration of roofing using a nailgun-equipped octocopter. Specifically, we consider the task in which a human or robot assistant has already placed a shingle, and the octocopter attaches the shingle to the roof. Fig. 1 shows the autonomous roofing sequence. The vehicle takes off per frame 1 and follows a prescribed trajectory through frame 2 to a hold waypoint at frame 3. The vehicle then must establish contact between the mounted nailgun and each of four nailing points as marked with a consistent force and sufficient accuracy to effectively fasten the shingle. The octocopter must also be capable of adjusting to different roof slopes while handling associated changes in applied forces.

This paper offers the following contributions:

1) Hardware integration for roof nailing via UAS.
2) Characterization of UAS waypoints, motions, and contact forces required for successful nail insertion.
3) The first experimental demonstration of autonomous roofing with a UAS.
4) Analysis of experimental nail placement accuracy and error sources to be addressed in future work.

Below, Section II reviews recent work in small multirotor aircraft guidance, control, and aerial manipulation. Sec. III presents our experimental system including a nailgun-equipped octocopter, avionics, and a slope-adjustable roof mock-up. Sec. IV defines our system model and roofing task sequence, while Sec. V describes our guidance algorithm and velocity profile computation for each trajectory segment. Experimental results are shown in Sec. VI. Secs. VII and VIII discuss nailing accuracy and conclusions, respectively.

II. Related Work

Aerial robots are capable of following complex 3D trajectories with high accuracy and support sufficient payload sizes for a range of applications. Ref. [5] provides a tutorial on modeling, estimation, and control of multirotor vehicles

*PhD Candidate, Robotics Institute, AIAA Student Member
†MS Student, Robotics Institute
‡PhD Candidate, Robotics Institute, AIAA Student Member
§MS Student, Robotics Institute
¶Professor, Aerospace Engineering and Robotics, AIAA Fellow

Copyright © 2021 by Matthew Romano, Yuxin Chen, Prince Kuevor, Owen Marshall, Ella Atkins.
Published by the American Institute of Aeronautics and Astronautics, Inc., with permission.

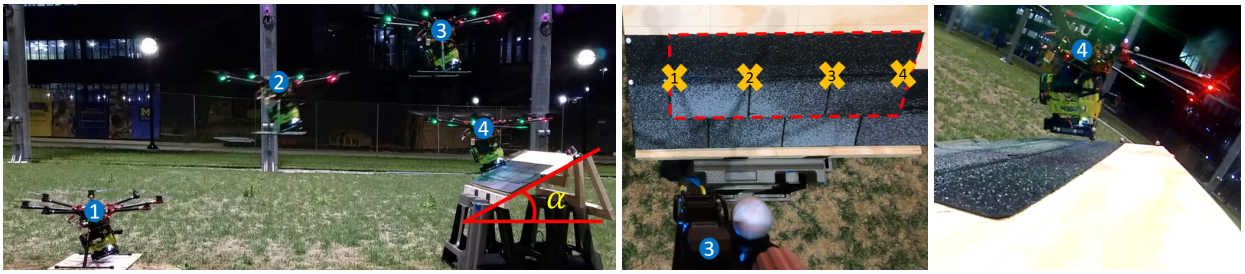

(a) Third person view **(b) Nailgun view** **(c) Roof board view**

Fig. 1 Autonomous roofing nailing sequence from three views. A) Third person camera view showing the vehicle at four time frames (denoted by the numbered blue circles). A roof mock-up is captured on the right at an inclination angle of α. B) Nailgun view during time frame 3. A pre-placed shingle is ready to be nailed; the four nailing points are shown with yellow crosses. C) Roof board view during time frame 4. Contact has been made and nailing is about to occur. A video of this sequence can be found at `https://youtu.be/0oOdiu5n3lQ`.

Downloaded by Matthew Romano on July 29, 2021 | http://arc.aiaa.org | DOI: 10.2514/6.2021-3211

with focus on quadrotors. In Ref. [6], the authors consider the aggressive flight of a quadrotor through a narrow gap using onboard sensing. They generate a trajectory that considers geometric, dynamic, and perception constraints and experimentally demonstrate their system with an 80% success rate on gaps up to 45 degrees. Ref. [7] details the formulation of an optimization problem for minimum snap trajectory generation and control for quadrotors. Given a set of 3-D positions and yaw angles at specified times, a trajectory is generated that satisfies velocity, acceleration, and input constraints while minimizing snap. A nonlinear controller is presented along with experimental results of a quadrotor flying through thrown and static hoops.

Aerial robots have recently been used for manipulation tasks. Unlike grounded robot arms, aerial manipulators do not have a fixed base and are subject to complex aerodynamic effects. Refs. [8] and [9] provide recent literature surveys of the field. In Ref. [10], the authors present a spray-painting quadrotor. The system consists of a quadrotor with a spray gun on a pan-tilt mechanism. Power and paint are supplied via tethers. The full system implementation and testing required modeling a 3D painting surface offline, generating the desired painted surfaces as well as robot commands, then actually applying paint to the surface. Ref. [11] considers the problem of landing a quadrotor on an inclined platform of a moving ground vehicle. A model predictive control (MPC) strategy is used for experimental demonstration. Ref. [1] describes an aerial manipulation system consisting of a helicopter with an attached seven degree of freedom industrial robotic arm. Analysis of dynamic coupling between helicopter and arm was performed, and a control approach to counteract this coupling was demonstrated in an object grasping task. Ref. [2] presents an aerial robot with door-opening capabilities using an initial perching approach to the door. Suction cups enable the vehicle to hang; a knob-twisting manipulator with appropriate rotor thrust are then coordinated to open the door.

This paper extends such work to autonomous nailing of roof shingles using an octocopter UAS. Specifically, we are inspired by workflow for the spray-painting quadrotor of Ref. [10]. Careful modelling and planning occurs before execution. Additionally, although nonlinear controllers provide certain benefits, we will be operating in a range of states and aggressiveness levels that do not require their use, so we utilize cascaded-PID control and focus research on planning, guidance, and experiment-based demonstration and analysis. Optimization-based trajectory planning was considered, but due to reliability concerns found through initial testing (e.g., local minima traps) we instead leveraged computationally-efficient quintic and quartic spline guidance strategies to smoothly connect trajectory segments.

III. System Description

The octocopter utilized for testing was a DJI Spreading Wings S1000 with weight capacity sufficient to carry an electric nailgun. The S1000 has eight 400kV 4114 Pro brushless DC motors each with 500W maximum power. 8kHz Electronic Speed Controllers (ESCs) drive the motors that turn pairs of 1552 foldable high strength plastic propellers [12]. A 6S 10000mAh LiPo battery powers the vehicle, which can achieve 10min of flight time with the 9.25kg gross takeoff weight including nailgun assembly.

Our testing nailgun was the RYOBI 18-Volt ONE+ Lithium-Ion Cordless AirStrike 18-Gauge Brad Nailer. Professional roofing nailguns use larger, flat head nails with air hose connection required. Our tetherless system is a prototype that allowed us to focus on autonomous operation. In practice, the octocopter would have a professional nailgun with an air

hose and power tether for extended endurance. The chosen nailgun came with built-in safety features that require a specific procedure to deploy a nail: 1) Press the tooltip (Figures 2a and 2b), 2) Push the trigger button, and 3) Nail by keeping the tooltip pressed for about 0.5s. To adapt step 2 for autonomous operation, a limit switch was added for feedback of the tooltip state. Additionally, the trigger was replaced with a relay controlled by our onboard electronics. While the vehicle follows its nailing trajectory, our software engages the relay whenever the limit switch is pressed. At all other times, the relay was not engaged, disabling the nailgun and preserving the original "contact" layer of safety. Figure 2c shows the nailgun mount. We designed a custom nailgun holder to mount the nailgun with adjustable angles corresponding to the available roof slopes: 0° (straight down), 15°, 30°, and 45°. All parts are 3D-printed.

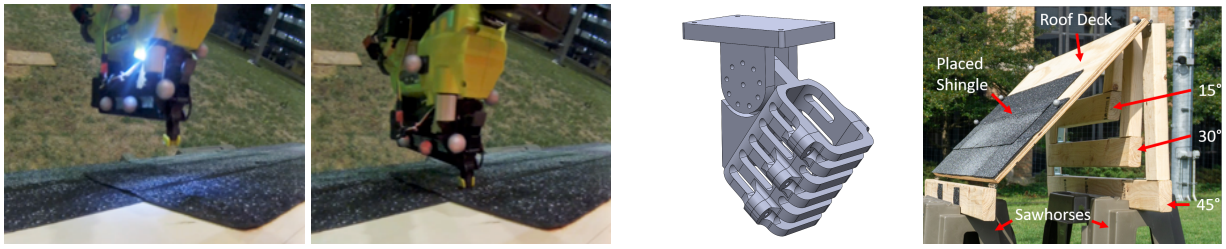

(a) Not Pressed, Light On **(b) Pressed, Light Off** **(c) Nailgun Mount** **(d) Roof mock-up.**

Fig. 2 Hardware description of nailgun and roof mock-up. a-b) Tooltip must be pressed to activate the relay and fire the nailgun. c) Adjustable angle nailgun mount. d) Adjustable angle roof mock-up.

To demonstrate our system, we constructed a roof mock-up per Fig. 2d. The roof deck is 3/4", 5-layer plywood with dimensions 2'×4'. This decking is connected with hinges to three different stands with heights that support four different roof slope angles (0°, 15°, 30°, and 45°). During experiments, the roof model is placed on two sawhorses with four sandbags to keep them stable. Half of the roof deck has attached shingles, and for each test a new shingle is placed but not yet nailed. For software, we used a modified version of Ardupilot (APM) running on an embedded BeagleBone Blue single-board Linux computer. Its cascaded proportional-integral-derivative (PID) controller tracks a preloaded trajectory using motion capture feedback in M-Air, Michigan's outdoor netted flight facility. See Sec. IV from Ref. [13] for further multicopter controller details.

IV. System Model

We defined a kinematic model including reference frames, transformations between reference frames, and relevant key points for the autonomous roofing problem. Figure 3a shows our defined reference frames including ground frame (G), roof frame (R), and vehicle frame (V). The ground frame follows a North-East-Down (NED) convention and is affixed to the takeoff position, which is also the motion capture origin. The roof frame origin is located at the lower left corner of the roof mockup which allows us to express the nailing points on the 2D roof surface with only $\mathbf{x}_R$ (vertical) and $\mathbf{y}_R$ (horizontal) values. The vehicle frame is attached to the center of the octocopter rotor plane.

Transforming points between reference frames was done with rigid body transformations. Define $\mathbf{r}_i^b \in \mathbb{R}^{3\times1}$ as a point, i, expressed in frame b. $\mathbf{r}_i^b$ can be transformed into frame a using a rigid body transformation as $\mathbf{r}_i^a = \mathbf{R}_b^a \mathbf{r}_i^b + \mathbf{t}_b^a$, where $\mathbf{R}_b^a \in SO(3)$ is a rotation matrix whose column vectors are the coordinates of the axes of frame b expressed relative to frame a, and $\mathbf{t}_b^a \in \mathbb{R}^{3\times1}$ is a translation vector that is the origin of frame b expressed in frame a. Rotation matrices were further decomposed with the use of Euler angles. Define an Euler angle rotation (ϕ,θ,ψ) of frame b relative to frame a as a rotation ψ (yaw) about the z-axis of frame a followed by rotation θ (pitch) about the current y-axis and finally rotation ϕ (roll) about the current x-axis such that

$$\mathbf{R}_b^a = \mathbf{R}_{z,\psi}\mathbf{R}_{y,\theta}\mathbf{R}_{x,\phi} = \begin{bmatrix} c_\psi c_\theta & c_\psi s_\theta s_\phi - c_\phi s_\psi & s_\psi s_\phi + c_\psi c_\phi s_\theta \\ c_\theta s_\psi & c_\psi c_\phi + s_\psi s_\theta s_\phi & c_\phi s_\psi s_\theta - c_\psi s_\phi \\ -s_\theta & c_\theta s_\phi & c_\theta c_\phi \end{bmatrix}.$$

For our system, define transformations for the vehicle relative to the ground frame as ($\mathbf{t}_V^G, \mathbf{R}_V^G = \mathbf{R}_{z,\psi_V}\mathbf{R}_{y,\theta_V}\mathbf{R}_{x,\phi_V}$) and roof relative to ground as ($\mathbf{t}_R^G, \mathbf{R}_R^G = \mathbf{R}_{z,\psi_R}\mathbf{R}_{y,\alpha}\mathbf{R}_{x,\phi_R}$). Both were obtained from motion capture with $\mathbf{R}_V^G$ also estimated from an onboard IMU. Note the definition of roof pitch as α per Fig. 1.

Downloaded by Matthew Romano on July 29, 2021 | http://arc.aiaa.org | DOI: 10.2514/6.2021-3211

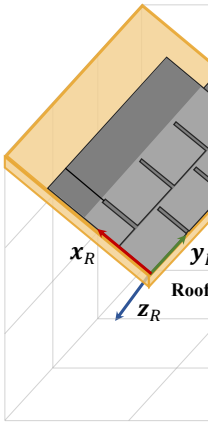

(a) Ta

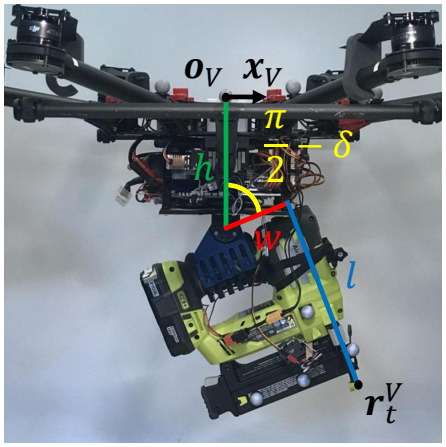

(b) Tooltip position in the vehicle frame.

Fig. 3 Reference frame definitions.

Nailing points were selected based on roofing industry specifications. Our experiments used three-tab shingles and the four-nail method as seen in Fig. 4 and explained in [14]. Nails should be placed on the shingle ideally just below the sealing strip and above the exposure cutouts (3cm gap). An optimal placement of the four nails is shown in Fig. 4. From this, define N nailing points ($N = 4$ in this case) in the roof frame as $\mathbf{r}_{n,i}^R = \begin{bmatrix} x_{n,i}^R & y_{n,i}^R & 0 \end{bmatrix}^T, i \in \{1, ..., N\}$, where $x_{n,i}^R$ and $y_{n,i}^R$ are the coordinates of the ith nailing point in $\mathbf{x}_R$ and $\mathbf{y}_R$ respectively. These can be converted to the ground frame with $\mathbf{r}_{n,i}^G = \mathbf{R}_R^G \mathbf{r}_{n,i}^R + \mathbf{t}_R^G$. Additionally, from Fig. 3b we can describe the tooltip position in the vehicle frame as

$$\mathbf{r}_t^V = \begin{bmatrix} w\cos\delta + l\sin\delta \\ 0 \\ h - w\sin\delta + l\cos\delta \end{bmatrix}, \tag{1}$$

where h, w, and l are fixed lengths and $\delta \in \{0°, 15°, 30°, 45°\}$ is the angle of the nailgun (shown at 30°). The tooltip position can be converted to the ground frame using $\mathbf{r}_t^G = \mathbf{R}_V^G \mathbf{r}_t^V + \mathbf{t}_V^G$. To insert a nail at position $\mathbf{r}_i^R$ in the roof frame, we must have $\mathbf{r}_t^G = \mathbf{r}_i^G$. Rearranging terms gives

$$\mathbf{t}_V^G = \mathbf{R}_R^G \mathbf{r}_i^R + \mathbf{t}_R^G - \mathbf{R}_V^G \mathbf{r}_t^V, \tag{2}$$

which defines the position of the vehicle in the ground frame ($\mathbf{t}_V^G$) for each tooltip position in the roof frame ($\mathbf{r}_i^R$).

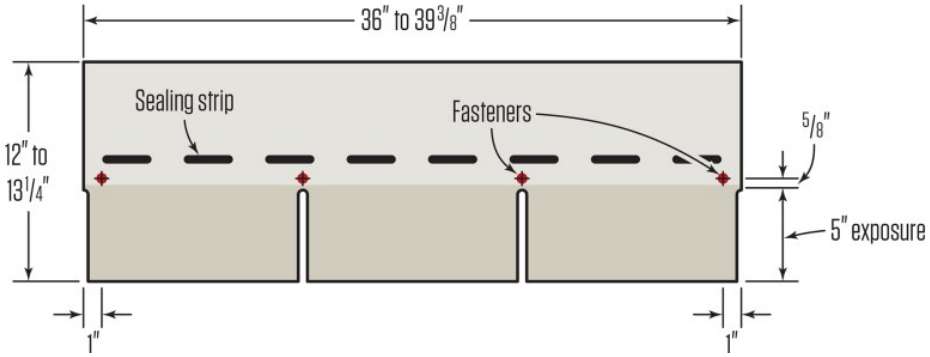

Fig. 4 The Four-Nail Method for Three-Tab Shingles. Nails should be positioned as shown, within a 3cm vertical gap between the sealing strip and the shingle cut-out [14].

Downloaded by Matthew Romano on July 29, 2021 | http://arc.aiaa.org | DOI: 10.2514/6.2021-3211

V. Guidance

Successful nail deployment requires the UAS to keep the tooltip at the nailing point while maintaining sufficient compression force until the nailgun fires. We achieved this goal with a tooltip trajectory for each nail point that starts at a safety point, $\mathbf{r}_{s,i}$, goes through the desired nailing point, $\mathbf{r}_{n,i}$, and ends at a "beyond point" $\mathbf{r}_{b,i}$. Fig. 5 shows the waypoint sequence flown to install four shingle nails. After the final nail is installed the UAS flies to a home waypoint for landing. The tooltip doesn't actually reach beyond point $\mathbf{r}_{b,i}$ but this position offset allows the cascaded PID controller to apply force in a controlled manner. $\mathbf{r}_{s,i}$ and $\mathbf{r}_{b,i}$ are obtained by shifting $\mathbf{r}_{n,i}$ up by d_s and down by d_b in the roof frame, respectively as $\mathbf{r}^R_{s,i} = \mathbf{r}^R_{n,i} - \begin{bmatrix}0 & 0 & d_s\end{bmatrix}^T, \forall i$ and $\mathbf{r}^R_{b,i} = \mathbf{r}^R_{n,i} + \begin{bmatrix}0 & 0 & d_b\end{bmatrix}^T, \forall i$, where d_s is the safety distance and d_b is the beyond distance. A piece-wise quartic spline (Sec. V.B) was used for the nailing trajectory from $\mathbf{r}_{s,i}$ to $\mathbf{r}_{b,i}$ with $v_f = 15$cm/s, $a_{max} = 10$cm/s^2, $d_s = 1$m, $d_b = 24$cm. Quintic splines (Sec. V.A) were used for the safety trajectory from $\mathbf{r}_{b,i}$ to $\mathbf{r}_{s,i+1}$ ($\mathbf{r}_{b,4}$ goes to $\mathbf{r}_{s,4}$) with zero velocity and acceleration at the endpoints. Lastly, a takeoff trajectory (takeoff point to $\mathbf{r}_{s,1}$), and a return and land trajectory ($\mathbf{r}_{s,4}$ to takeoff point) also used quintic splines for

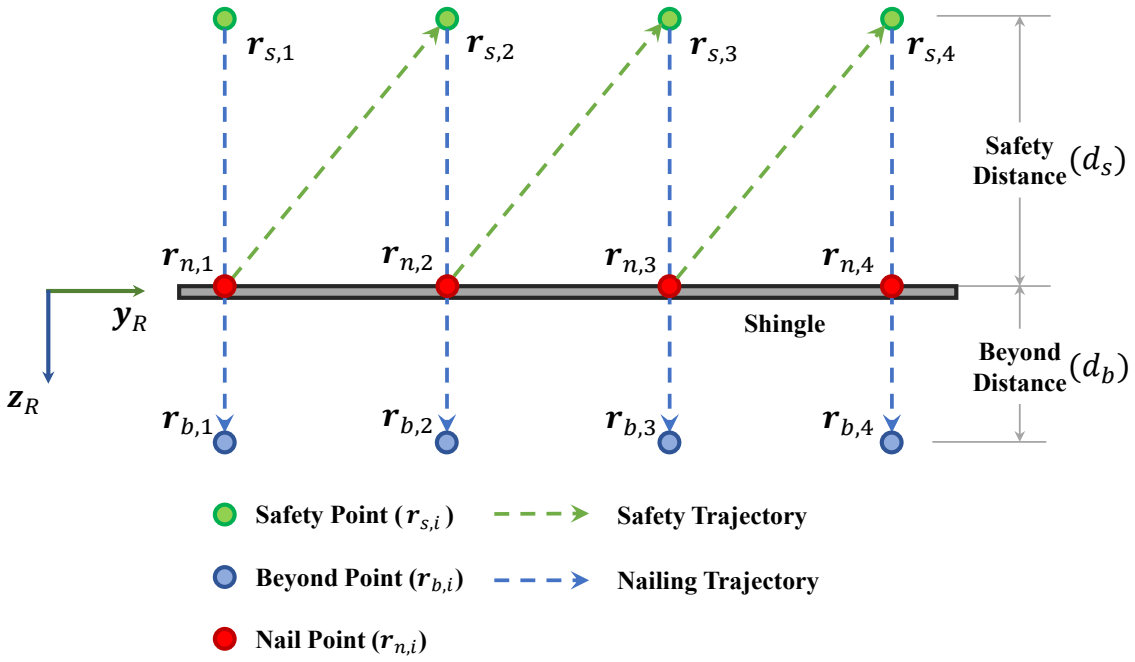

Fig. 5 Guidance used for autonomous nailing (in the roof frame). A piece-wise quartic spline is used for nailing trajectories (blue), and quintic spline guidance is used for safety trajectories (green).

A. Quintic Spline Method

Takeoff, landing, and safety trajectories used quintic splines to create smooth trajectories between waypoints. A quintic spline is defined as a fifth order polynomial of the form $r_i(t) = \sum_{j=0}^{5} a_{j,i} t^j$, where $r_i(t)$ is the trajectory function at travel time t in the ith direction, and $a_{j,i}$ is the jth coefficient of the spline in the ith direction. To solve for the six coefficients, boundary conditions at initial and final times t_0 and t_f, respectively, can be provided. The coefficients can

Downloaded by Matthew Romano on July 29, 2021 | http://arc.aiaa.org | DOI: 10.2514/6.2021-3211

then be obtained by solving

$$\begin{bmatrix} 1 & t_i & t_0^2 & t_0^3 & t_0^4 & t_0^5 \\ 0 & 1 & 2t_0 & 3t_0^2 & 4t_0^3 & 5t_0^4 \\ 0 & 0 & 2 & 6t_0 & 12t_0^2 & 20t_0^3 \\ 1 & t_f & t_f^2 & t_f^3 & t_f^4 & t_f^5 \\ 0 & 1 & 2t_f & 3t_f^2 & 4t_f^3 & 5t_f^4 \\ 0 & 0 & 2 & 6t_f & 12t_f^2 & 20t_f^3 \end{bmatrix} \begin{bmatrix} a_{0,i} \\ a_{1,i} \\ a_{2,i} \\ a_{3,i} \\ a_{4,i} \\ a_{5,i} \end{bmatrix} = \begin{bmatrix} r_i(t_0) \\ \dot{r}_i(t_0) \\ \ddot{r}_i(t_0) \\ r_i(t_f) \\ \dot{r}_i(t_f) \\ \ddot{r}_i(t_f) \end{bmatrix}. \tag{3}$$

As noted above, we use $\dot{r}_i(t_0) = \dot{r}_i(t_f) = 0$ and $\ddot{r}_i(t_0) = \ddot{r}_i(t_f) = 0$ for all quintic spline trajectories.

B. Piece-wise Quartic Spline

To ensure reliable tooltip interaction with the shingle and consistent firing we designed a piece-wise quartic spline for the nailing trajectory from $\mathbf{r}_{s,i}$ to $\mathbf{r}_{b,i}$. The goal was to have the tooltip start from rest, smoothly accelerate (with max acceleration a_{max}) to a specified velocity, v_f, contact the nailing point at this velocity, and finally continue pushing into the nailing point to allow for firing.

We first calculated the trajectory in 1D before lifting it into 3D and considered a trajectory of the form $s_1(t) = b_3t^3 + b_4t^4$. This choice allows us to apply constraints similar to how we did for a quintic spline to shape the trajectory to our liking. By omitting the first three terms of a general quartic function we effectively constrain the initial position, velocity, and acceleration to zero. Next, we constrain the acceleration profile with $\ddot{s}_1(t_{ext}) = a_{max}$ and $\ddot{s}_1(t_1) = 0$, where $t_{ext} = -\frac{b_3}{4b_4}$ is where the extrema of $\ddot{s}_1(t)$ occurs and t_1 is the time required to reach the desired velocity. Lastly, we constrain the final velocity as $\dot{s}_1(t_1) = v_f$ then solve for the parameters as $b_3 = \frac{4a_{max}^2}{9v_f}$, $b_4 = -\frac{4a_{max}^3}{27v_f^2}$, and $t_1 = \frac{3v_f}{2a_{max}}$. The remaining trajectory has constant velocity until t_f, where $t_f = t_1 + \frac{\Delta s - s_1(t_1)}{v_f}$ and $\Delta s = ||\mathbf{r}_{b,i} - \mathbf{r}_{s,i}||$. The full trajectory in 1D is

$$s(t) = \begin{cases} b_3t^3 + b_4t^4 & 0 \le t \le t_1 \\ s_1(t_1) + v_f\ (t - t_1) & t_1 \le t \le t_f, \end{cases} \tag{4}$$

and can be lifted into 3D from $\mathbf{r}_{s,i}$ to $\mathbf{r}_{b,i}$ as

$$\mathbf{r}(t) = \frac{\mathbf{r}_{b,i} - \mathbf{r}_{s,i}}{||\mathbf{r}_{b,i} - \mathbf{r}_{s,i}||} s(t) + \mathbf{r}_{s,i}, 0 \le t \le t_f. \tag{5}$$

We chose $a_{max} = 10\text{cm/s}^2$ and $d_s = 1\text{m}$ based on intuition since using conservative values would slow the trajectory down but wouldn't affect the tooltip interaction, which was the main focus. A beyond distance of $d_b = 24\text{cm}$ was set after some experimentation to make sure enough force was applied after making contact, however, choosing a proper desired velocity, v_f, was the most important for nailing success. An approach that is too slow or too fast would cause bouncing of the tooltip off of the shingle and therefore inaccurate nailing. Therefore, we guided our parameter selection by modelling the tooltip as a spring with attached mass and considered contacting the shingle as an elastic collision. Thus, we assumed conservation of energy during tooltip compression to obtain the desired velocity magnitude for each boundary condition.

$$\frac{1}{2}mv_1^2 = \frac{1}{2}\cancel{mv_2^2}^{\,0} + \frac{1}{2}kc^2 \Rightarrow v_1 = \sqrt{\frac{k}{m}}c, \tag{6}$$

where m is the total system mass, v_1 is the velocity before nailgun tip compression, v_2 is the final velocity after compression (zero), k is the spring constant, and c is the compression length. The tooltip spring constant was measured by vertically pushing down the nailgun on a scale until it compressed. Compression distance was measured with a caliper. The remaining parameters are listed in Table 1 with a resulting desired nailing velocity of 13.6cm/s. We chose 15cm/s for experiments to ensure sufficient compression for nail release.

Downloaded by Matthew Romano on July 29, 2021 | http://arc.aiaa.org | DOI: 10.2514/6.2021-3211

Table 1 Tooltip and Nailing Velocity Parameters

Notation	Name	Value
F	Spring Force	25N
c	Compression Distance	7mm
k	Spring Const.	3.5kN/m
m_o	Octocopter Mass	4.8kg
m_b	Battery Mass	1.4kg
m_n	Nailgun Mass	3.0kg
m	Total Mass	9.2kg
v_1	Calculated Velocity	13.6cm/s

VI. Results

A total of four roof angles α were tested: 0°, 15°, 30°, and 45°. However, the 45° case was unsuccessful in our nailing attempts due in part to the tooltip slipping down the roofing board and partly due to the propellers getting too close to the board when nailing. For the three remaining angles, a total of 16 full shingle nailing experiments were performed with measured data over the course of several flight test days. A breakdown of the conditions can be seen in Table 2. For each experiment, four nailing attempts were made giving a total of 64 nailing attempts.

Table 2 Test conditions and nail deployments by test set.

Test Set	Windy	PID Gains	0°	15°	30°	Nails Deployed	Nails Attempted
A	No	set2	2	2	2	24	24
B	No	set2	0	5	0	17	20
C	Yes	set2	1	1	0	8	8
D	No	set2	0	0	1	4	4
E	No	set1	1	1	0	8	8
All	**Yes/No**	**set1/set2**	**4**	**9**	**3**	**61**	**64**

Define horizontal error as $e_h = y_d^R - y_a^R$ and vertical error as $e_v = x_d^R - x_a^R$, where x_d^R and y_d^R are the desired nailing positions and x_a^R and y_a^R are where the nails actually were placed. After each experiment, the error in placement of each inserted nail was measured with respect to a shingle outline on the back side of the roof structure with marked setpoints. Figure 6 shows nailing accuracy for all tests. Define the range for a set of data as the largest value minus the smallest value. Horizontal error trends indicate range decreases as the roof angle α increases. For 0° there is low precision with a range of 10.4cm. For 30° the precision is high with a range of 2.6cm and the accuracy is also high with a median of 0.0cm. In vertical error there is a trend in accuracy. As the angle increases so does the median (-0.8cm at 0°, 3.4cm at 15°, and 6.4cm at 30°).

During testing, we were noticing the vertical bias in nail placements (seen in Fig. 6b) and felt that a constant offset bias calculated experimentally would be reasonable over time. Therefore, for some of the test sets the desired points were shifted a few centimeters in the roof frame vertical direction to compensate. Due to our guidance method, the nailing trajectory is orthogonal to the roof plane, which means that shifts along the roof plane (as we did) should not affect the error obtained from a geometric standpoint. Figure 7 shows our nail deployment results on a shingle plot by roof slope α. To compensate for the slightly differing setpoints (noted above), all test set desired points are shifted to be aligned and their associated nailing points are shifted the same amount. This preserves all errors from the true experimental data and also allows trends to be more easily noticed. In particular, the vertical error can be seen to increase as the roof slope increases with groupings of nail insertion points fairly close together. To build off of the idea of a consistent vertical bias, Fig. 8 displays the same nailing points adjusted by the mean error for each angle (-1.5mm for 0°, 31.7mm for 15°, and 60.6mm for 30°). If these shifts were applied to the desired nailing points during initial experiments, the observed systematic bias could be compensated and only the spread of the points would matter for nailing. Further testing would be required to determine bias source(s) and repeatability.

Figures 9, 10, and 11 show the position, velocity, and orientation data from an instance of test set A at roof slope 30°.

Downloaded by Matthew Romano on July 29, 2021 | http://arc.aiaa.org | DOI: 10.2514/6.2021-3211

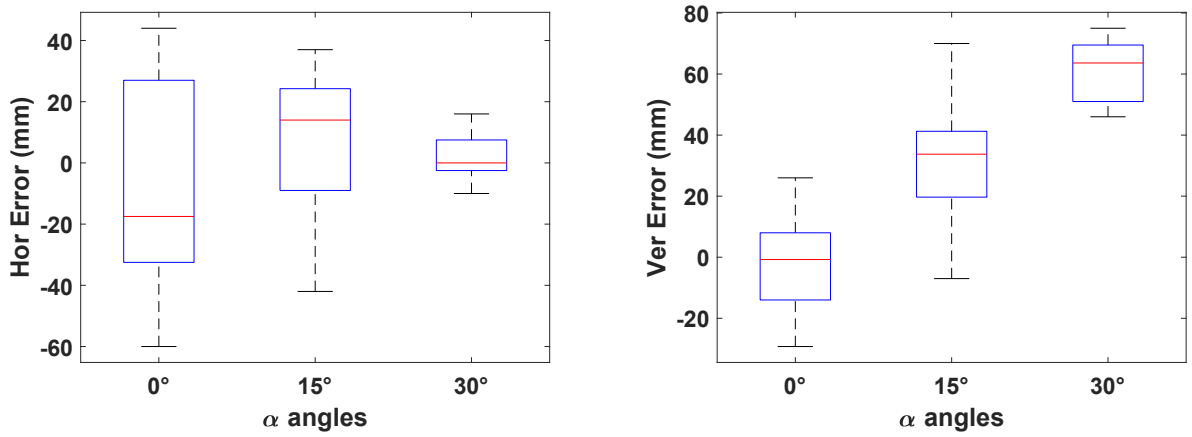

(a) Horizontal Error **(b) Vertical Error**

Fig. 6 Nail placement error box plots by angle for all tests.

A noticeable disturbance can be seen at about 22s when the vehicle contacts nail point 1 and the reference trajectory is no longer accurately followed. This divergence is to allow for the tooltip to be pressed into the shingle towards the beyond point via the PID controller. Also note the small (2-3cm) error in x position immediately prior to nailing. We would expect this effect to be more significant at higher roof angles due to gravity-based tooltip slip and decreased octocopter authority in compression while maintaining a stable hover.

VII. Discussion

Nailing results from Sec. VI offer evidence that our system can properly nail shingles to within a vertical 3cm gap. For all 12 nails at 30°, our vertical range of error was only 2.9cm with a bias of 60.6mm. Additionally, we have demonstrated a method to correct for this bias indicating that if the bias is properly accounted for, and we maintain our precision, we can accurately nail a shingle onto a roof at 30°. Surprisingly, our range in vertical error was worse for 0° (5.5cm) and 15° (7.7cm) for all tests.

Fig. 6b shows that median vertical error increases as roofing angle increases. One probable source of this vertical error is a systematic 2-3cm x position error from the cascaded PID controller combined with a nearly zero z position error. Additionally, we planned for a specific vehicle attitude during nailing. In the piece-wise quartic spline trajectory, attitude is not quite level (as it would be for ideal hover); disturbance rejection yielded some uncertainty in vehicle attitude at the time of nailgun contact. Modelling errors in nailgun kinematics may also have contributed to the vertical error trend. For each roof angle, the nailgun angle is also changed, so nailgun modelling errors would be consistent for a particular angle but could differ as a function of contact angle. Also, the nailgun was modelled as a rigid body, when in fact there was a small amount of movement that occurred between the actual nailgun and the mount. Ground effect could have played a role in the vertical error at non-zero roof angles. The front propellers are much closer to the roof than the rear propellers which could cause asymmetrical force generation.

Another trend can be seen in Fig. 7a. The first two nailing points on the left are biased to the left and the last two are biased to the right. Ground effect may have given the propellers directly over the flat roof more force than the propellers directly over the ground. This asymmetric disturbance would cause the vehicle to initially roll slightly away from the roof center before the controller compensates to roll slightly towards the roof center. Since the tooltip is at an offset from the roll axis this would cause an outward shift in the actual nailing position. Also, this effect would be greater for the roof nailing points nearest to the edges, which does appear true.

Fig. 6a shows a third trend in which the range of horizontal error decreases as roofing angle increases. This may be explained by asymmetric disturbances from ground effect near the roof edge as described above. At 0° the roof is flat, ground effect is strong, and horizontal error range is large. As the roof angle increases, airflow is less impeded by the roof, ground effect weakens, and horizontal error range decreases. Further analysis and testing would be needed to explore these error sources in more depth.

At a real roofing site no motion capture system would be available. Instead, an onboard sensing system could be

Downloaded by Matthew Romano on July 29, 2021 | http://arc.aiaa.org | DOI: 10.2514/6.2021-3211

Downloaded by Matthew Romano on July 29, 2021 | http://arc.aiaa.org | DOI: 10.2514/6.2021-3211

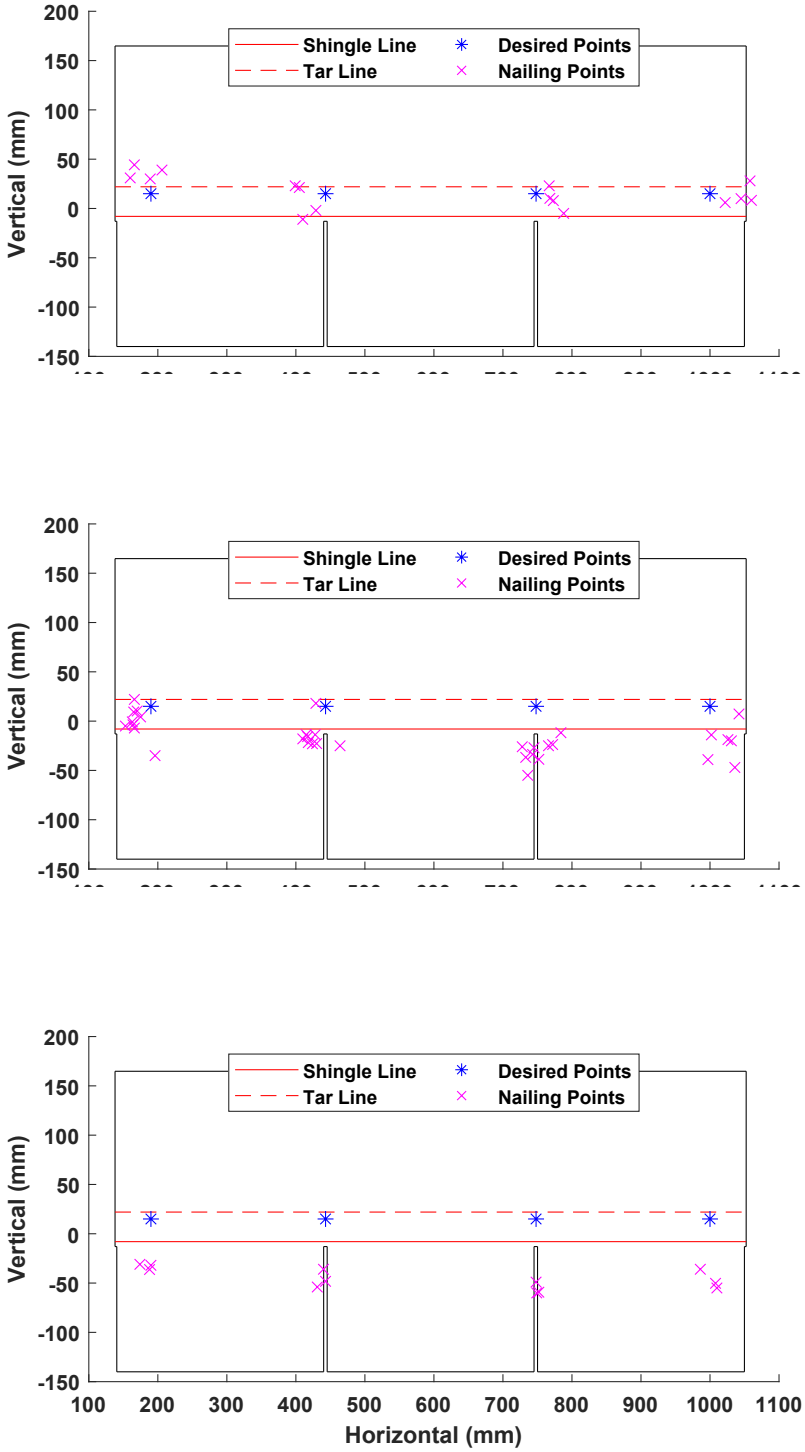

(c) α = 30 degrees

Fig. 7 Nail placements for all test sets at each roof slope α. Nailing points were shifted to align all desired points (which differed slightly between test sets) to accurately display errors.

Downloaded by Matthew Romano on July 29, 2021 | http://arc.aiaa.org | DOI: 10.2514/6.2021-3211

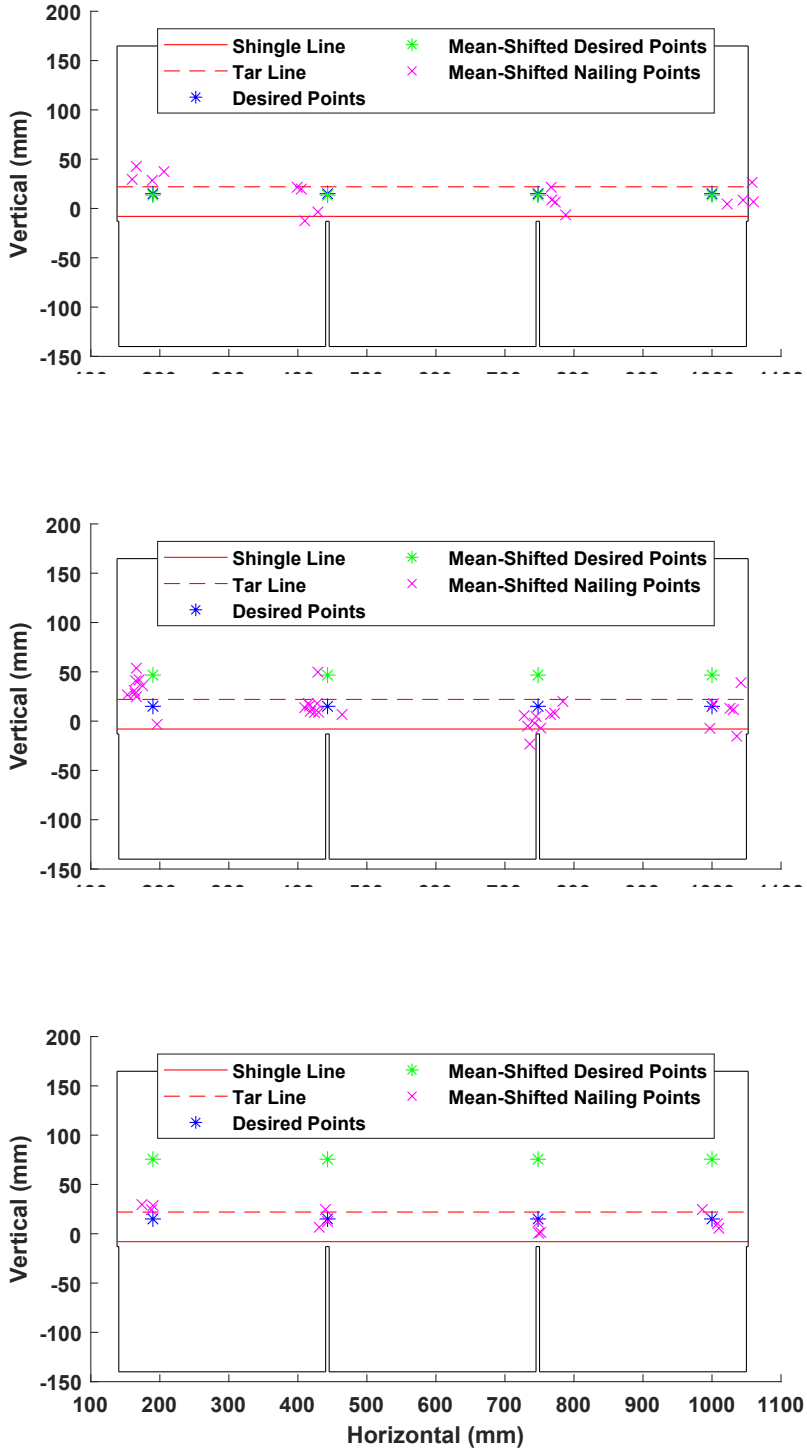

(c) α = 30 degrees

Fig. 8 Nail placements with vertical position shifted by the mean error of each roof angle α. No changes were made in horizontal positions.

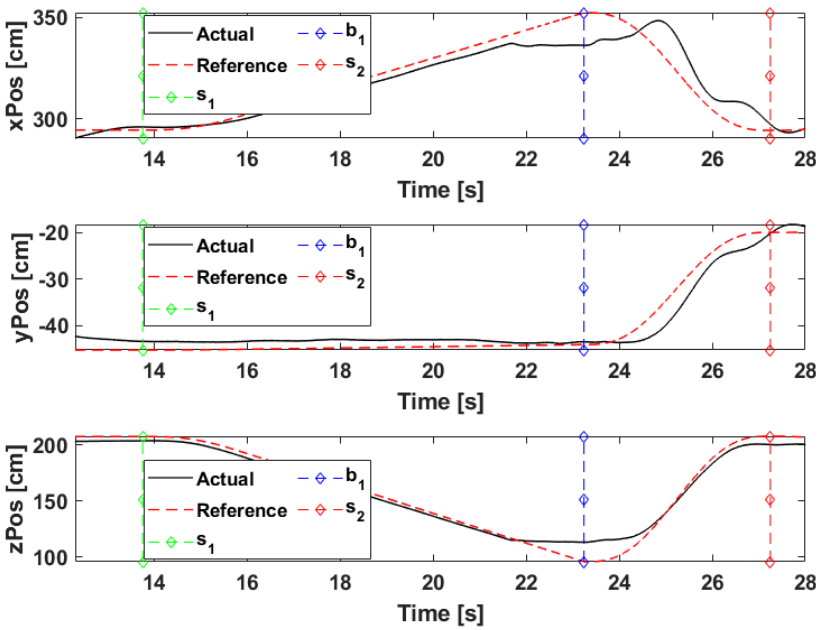

Fig. 9 Position plot for a 30° instance from test set A. At about 22s, contact is made and the z and x positions diverge from desired while nailing occurs.

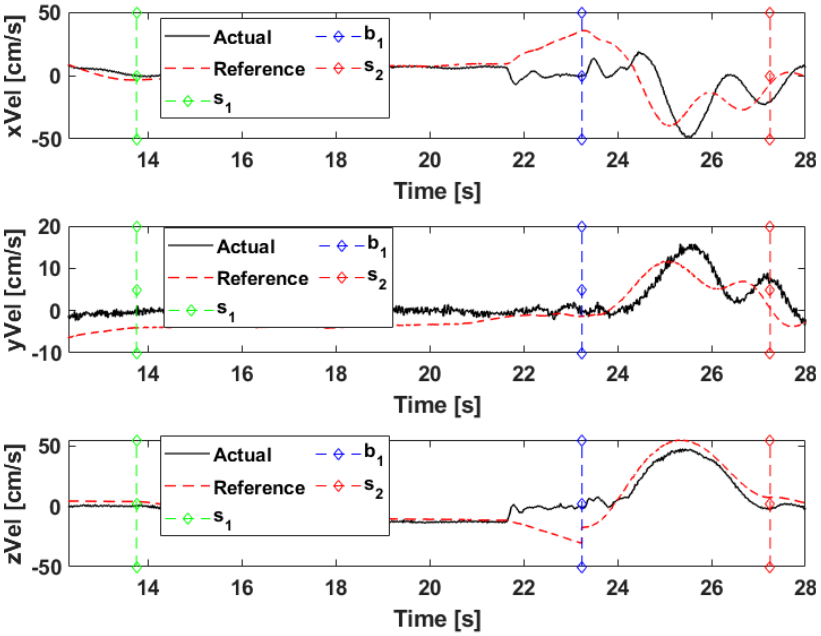

Fig. 10 Horizontal error for a 30° instance from test set A. At about 22s, contact is made and the z and x velocities diverge from desired to near 0 while nailing occurs.

Downloaded by Matthew Romano on July 29, 2021 | http://arc.aiaa.org | DOI: 10.2514/6.2021-3211

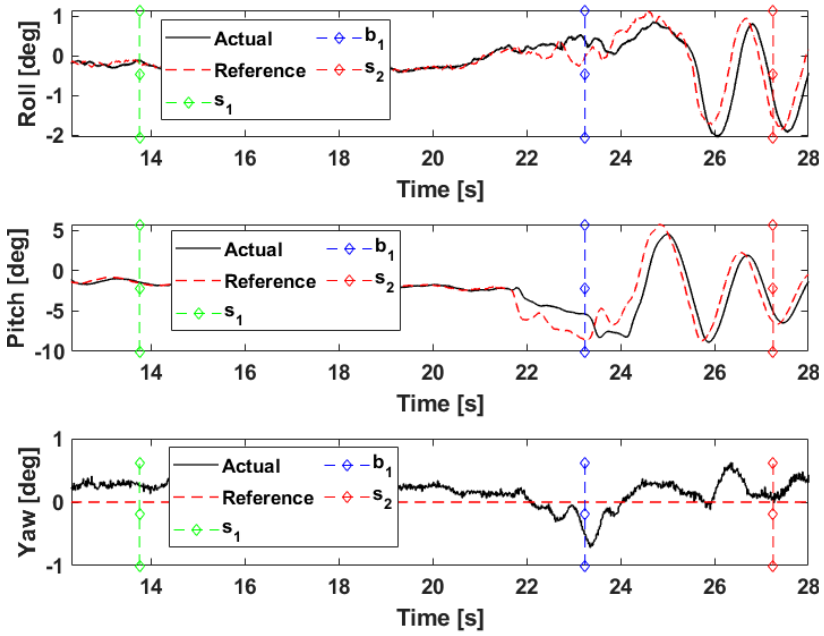

Fig. 11 Attitude plot for a 30° instance from test set A. At about 22s, contact is made and the vehicle leans into the roof, changing pitch from about -2° to -8°.

used to recognize shingle outlines on the approach trajectory to obtain accurate state estimation. Additionally, upgrading the system to a professional nailgun with an air hose and power tether would enable extended duration flights and insertion of proper large-head roofing nails. Even with our current octocopter platform a pneumatic nailgun would be feasible since power and air compression could be offloaded through tethers and a pneumatic nailgun has similar mass to the electric model. Other roofing tasks are also subject to aerial vehicle support, e.g., carrying lightweight supplies to roofers as needed.

VIII. Conclusion

This paper has presented the first experimental demonstration of an autonomous UAV roof nailing system. The nailing problem was described and translated to an integrated octocopter-nailgun roofing platform. Waypoint-based guidance offering the required nailing contact force was demonstrated. Autonomous nailing was successfully achieved at roof angles between 0° and 30°, but the 3cm vertical error tolerance was only reliably met at 30°. Several unexpected trends in nailing accuracy were uncovered and potential sources of error, including complex aerodynamic effects, were discussed. Future work includes extension to pneumatic air gun, power tether, and vision/depth based localization system.

Acknowledgements

This work was supported in part by National Science Foundation (NSF) Grant CNS 1739525.

References

[1] Huber, F., Kondak, K., Krieger, K., Sommer, D., Schwarzbach, M., Laiacker, M., Kossyk, I., Parusel, S., Haddadin, S., and Albu-Schaffer, A., "First analysis and experiments in aerial manipulation using fully actuated redundant robot arm," *2013 IEEE/RSJ International Conference on Intelligent Robots and Systems*, IEEE, 2013. doi:10.1109/iros.2013.6696848, URL `http://dx.doi.org/10.1109/IROS.2013.6696848`.

[2] Tsukagoshi, H., Watanabe, M., Hamada, T., Ashlih, D., and Iizuka, R., "Aerial manipulator with perching and door-opening capability," *2015 IEEE International Conference on Robotics and Automation (ICRA)*, IEEE, 2015. doi:10.1109/icra.2015.7139845, URL `http://dx.doi.org/10.1109/ICRA.2015.7139845`.

Downloaded by Matthew Romano on July 29, 2021 | http://arc.aiaa.org | DOI: 10.2514/6.2021-3211

[3] Geng, J., and Langelaan, J. W., "Implementation And Demonstration Of Coordinated Transport Of A Slung Load By A Team Of Rotorcraft," *AIAA Scitech 2019 Forum*, American Institute of Aeronautics and Astronautics, 2019. doi:10.2514/6.2019-0913, URL http://dx.doi.org/10.2514/6.2019-0913.

[4] U.S. Bureau of Labor Statistics, "Hours-based fatal injury rates by industry, occupation, and selected demographic characteristics, 2018," , ???? Retrieved from https://www.bls.gov/iif/oshcfoi1.htm#rates.

[5] Mahony, R., Kumar, V., and Corke, P., "Multirotor Aerial Vehicles: Modeling, Estimation, and Control of Quadrotor," *IEEE Robotics and Automation Magazine*, Vol. 19, No. 3, 2012, p. 20–32. doi:10.1109/mra.2012.2206474, URL http://dx.doi.org/10.1109/MRA.2012.2206474.

[6] Falanga, D., Mueggler, E., Faessler, M., and Scaramuzza, D., "Aggressive quadrotor flight through narrow gaps with onboard sensing and computing using active vision," *2017 IEEE International Conference on Robotics and Automation (ICRA)*, IEEE, 2017. doi:10.1109/icra.2017.7989679, URL http://dx.doi.org/10.1109/ICRA.2017.7989679.

[7] Mellinger, D., and Kumar, V., "Minimum snap trajectory generation and control for quadrotors," *2011 IEEE International Conference on Robotics and Automation*, IEEE, 2011. doi:10.1109/icra.2011.5980409, URL http://dx.doi.org/10.1109/ICRA.2011.5980409.

[8] Ruggiero, F., Lippiello, V., and Ollero, A., "Aerial Manipulation: A Literature Review," *IEEE Robotics and Automation Letters*, Vol. 3, No. 3, 2018, p. 1957–1964. doi:10.1109/lra.2018.2808541, URL http://dx.doi.org/10.1109/LRA.2018.2808541.

[9] Bonyan Khamseh, H., Janabi-Sharifi, F., and Abdessameud, A., "Aerial manipulation—A literature survey," *Robotics and Autonomous Systems*, Vol. 107, 2018, p. 221–235. doi:10.1016/j.robot.2018.06.012, URL http://dx.doi.org/10.1016/j.robot.2018.06.012.

[10] Vempati, A. S., Kamel, M., Stilinovic, N., Zhang, Q., Reusser, D., Sa, I., Nieto, J., Siegwart, R., and Beardsley, P., "PaintCopter: An Autonomous UAV for Spray Painting on Three-Dimensional Surfaces," *IEEE Robotics and Automation Letters*, Vol. 3, No. 4, 2018, p. 2862–2869. doi:10.1109/lra.2018.2846278, URL http://dx.doi.org/10.1109/LRA.2018.2846278.

[11] Vlantis, P., Marantos, P., Bechlioulis, C. P., and Kyriakopoulos, K. J., "Quadrotor landing on an inclined platform of a moving ground vehicle," *2015 IEEE International Conference on Robotics and Automation (ICRA)*, IEEE, 2015. doi:10.1109/icra.2015.7139490, URL http://dx.doi.org/10.1109/ICRA.2015.7139490.

[12] DJI, "Spreding Wings S1000 User Manual," http://dl.djicdn.com/downloads/s1000/en/S1000_User_Manual_v1.10_en.pdf, 2014.

[13] Romano, M., Kuevor, P., Lukacs, D., Marshall, O., Stevens, M., Rastgoftar, H., Cutler, J., and Atkins, E., "Experimental Evaluation of Continuum Deformation with a Five Quadrotor Team," *2019 American Control Conference (ACC)*, IEEE, 2019, pp. 2023–2029.

[14] Staff, J., "Asphalt Roof Shingling Basics," https://www.jlconline.com/training-the-trades/asphalt-roof-shingling-basics_o?o=0, 2018.

Downloaded by Matthew Romano on July 29, 2021 | http://arc.aiaa.org | DOI: 10.2514/6.2021-3211